Phase behavior of ionic liquid crystals

S. Kondrat, M. Bier, and L. Harnau[*]

Max-Planck-Institut für Metallforschung, Heisenbergstr. 3, D-70569 Stuttgart, Germany,
and Institut für Theoretische und Angewandte Physik,
Universität Stuttgart, Pfaffenwaldring 57, D-70569 Stuttgart, Germany [*]

(Dated: April 16, 2010)

Bulk properties of ionic liquid crystals are investigated using density functional theory. The liquid crystal molecules are represented by ellipsoidal particles with charges located in their center or at their tails. Attractive interactions are taken into account in terms of the Gay-Berne pair potential. Rich phase diagrams involving vapor, isotropic and nematic liquid, as well as smectic phases are found. The dependence of the phase behavior on various parameters such as the length of the particles and the location of charges on the particles is studied.

I. INTRODUCTION

The transportation of charges[1,2] and ions[3,4] in liquid crystals has attracted much attention because these materials are expected to serve as anisotropic conductors due to their self-organized structures. For this purpose the design and control of molecular interactions and microphase-segregated structures in ionic liquid crystals is essential. Moreover, the macroscopic orientation of self-organized monodomains plays an important role in the improvement of the conducting properties because the boundaries in randomly oriented polydomains disturb high and anisotropic transportation of charges and ions. Ionic liquid crystals can also be used as ordered solvents or organized reaction media. In these anisotropic solvents other chemo- and regioselectivities besides those in conventional solvents can be obtained for several types of reactions.

Various types of ionic liquid crystals have been prepared. The ionic liquid crystals based on imidazolium or pyridinium salts containing weakly coordinating anions such as BF_4^- and PF_6^- are representative due to their thermal and electrochemical stabilities.[5-10] In these and related materials the liquid crystalline phases are induced by microphase segregation of ionic moieties of long alkyl or perfluoroalkyl chains. The types of liquid crystalline phases depend on the molecular shape and location of the ionic parts on the molecules. Many ionic molecules containing single side chains form smectic structures. The influence of the anion type and chain length on the liquid crystalline phases has been investigated for 1-alkyl-3-methylimidazolium salts.[6,11,12] Very recently an efficient synthetic route towards calamitic guanidinium salts has been developed.[13] These guanidinium salts exhibit stable mesophases. Metal-based ionic liquid crystals containing a tetrahalometalate ion and N-alkylpyridinium salts exhibit a variety of liquid crystalline phases ranging from smectic to columnar or even cubic phases.[14,15] These metal-based materials can exhibit interesting properties as metal complexes such as chromism, magnetism, polarizability, redox behavior, and catalysis.

Thermotropic columnar liquid crystalline phases are formed by self-organization of fan-shaped imidazolium molecules.[16] In these phases the imidazolium parts form one-dimensional paths inside the columns. These columnar materials are macroscopically aligned by shearing on the glass substrate. Taubert described the use of an ionic liquid crystal as a template to synthesize CuCl nanoplatelets.[17,18] The platelets formed in the mesophase are relatively large and interconnected, whereas smaller platelets without permanent junction were formed in the isotropic liquid. Moreover, it has been shown that ionic liquids containing a guanidinium moiety tethered to a pentaalkyloxytriphenylene unit form platelike structures and columnar mesophases.[19]

In a recent review, Binnemanns has discussed many experimental studies that have been devoted to the synthesis and properties of ionic liquid crystals.[20] In particular he comes to the conclusion that theories that can explain the influence of the anisotropic charge distribution on the mesophase stability on ionic liquid crystals are still lacking. The aim of the present paper is to provide theoretical insight into the underlying mechanisms responsible for the formation of bulk liquid crystalline phases in ionic liquids. In Sec. II we define the system under consideration, and we describe the density functional theory. Representative phase diagrams and order parameter profiles are presented in Sec. III. Our results are summarized in Sec. VI.

II. MODEL

In this section we outline some points of the basic description of our model of ionic liquid crystals, and we record some details about the density functional theory.

A. Intermolecular pair potential

The intermolecular pair potential is expressed as a sum of the contribution due to excluded-volume interactions and the contribution due to long-ranged interactions:

$$U(\mathbf{r}_{12}, \boldsymbol{\omega}_1, \boldsymbol{\omega}_2) = \begin{cases} \infty, & r_{12} < R\,\sigma(\hat{\mathbf{r}}_{12}, \boldsymbol{\omega}_1, \boldsymbol{\omega}_2) \\ U_{GB}(\mathbf{r}_{12}, \boldsymbol{\omega}_1, \boldsymbol{\omega}_2) + U_{CO}(\mathbf{r}_{12}, \boldsymbol{\omega}_1, \boldsymbol{\omega}_2), & r_{12} \geq R\,\sigma(\hat{\mathbf{r}}_{12}, \boldsymbol{\omega}_1, \boldsymbol{\omega}_2) \end{cases} . \tag{1}$$

Here the pair potential $U(\mathbf{r}_{12}, \boldsymbol{\omega}_1, \boldsymbol{\omega}_2)$ between particles 1 and 2 is written as a function of the intermolecular vector $\mathbf{r}_{12}$ between the centers of mass of the two particles, and their orientations $\boldsymbol{\omega}_1$ and $\boldsymbol{\omega}_2$, where $r_{12} = |\mathbf{r}_{12}|$ is the magnitude of $\mathbf{r}_{12} = \mathbf{r}_2 - \mathbf{r}_1$ (see Fig. 1). The contact distance $R\,\sigma(\hat{\mathbf{r}}_{12}, \boldsymbol{\omega}_1, \boldsymbol{\omega}_2)$ depends on the orientations of both particles and on the unit vector $\hat{\mathbf{r}}_{12} = \mathbf{r}_{12}/r_{12}$ between their centers.
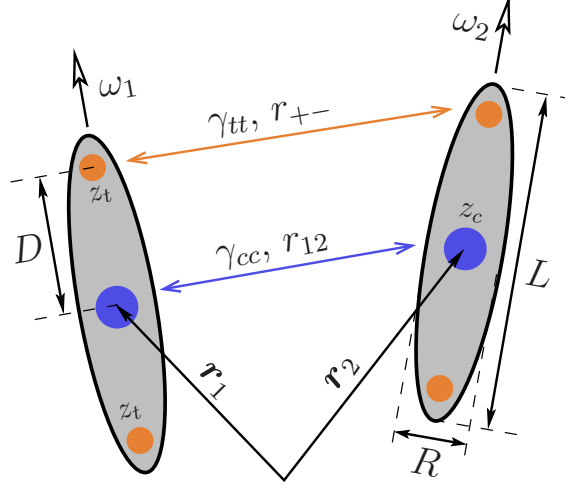

FIG. 1: Schematic side view of two prolate ellipsoids with orientations $\boldsymbol{\omega}_1$ and $\boldsymbol{\omega}_2$. The centers of mass of the ellipsoids are located at $\mathbf{r}_1$ and $\mathbf{r}_2$, respectively, where $r_{12} = |\mathbf{r}_1 - \mathbf{r}_2|$. Only the projections of the ellipsoids on the plane of the figure are shown and the centers and main symmetry axes of the ellipsoids are chosen to lie within the plane of the figure. R is the cross-sectional diameter of the ellipsoids and L is the particle length. The full circles mark the location of possible charges with valencies z_c and z_t in the center of the ellipsoids and at the tails at a distance D from the center, respectively. The energy scale of the Coulomb pair interaction acting between charged tails and between charged centers are denoted as γ_{tt} and γ_{cc} (see Eqs. (6) and (8)). In addition there is a corresponding Coulomb pair interaction acting between charged tails and centers.

We use the well-known Gay-Berne pair potential as a generalization of the Lennard-Jones pair potential to fluids consisting of nonspherical particles (see, e.g., Refs.[21–26] and references therein):

$$\begin{aligned} U_{GB}(\mathbf{r}_{12}, \boldsymbol{\omega}_1, \boldsymbol{\omega}_2) &= 4\epsilon(\hat{\mathbf{r}}_{12}, \boldsymbol{\omega}_1, \boldsymbol{\omega}_2) \\ &\times \left[\left(\frac{r_{12}}{R_0} - \sigma(\hat{\mathbf{r}}_{12}, \boldsymbol{\omega}_1, \boldsymbol{\omega}_2) + 1 \right)^{-12} - \left(\frac{r_{12}}{R_0} - \sigma(\hat{\mathbf{r}}_{12}, \boldsymbol{\omega}_1, \boldsymbol{\omega}_2) + 1 \right)^{-6} \right], \end{aligned} \tag{2}$$

$$\sigma(\hat{\mathbf{r}}_{12}, \boldsymbol{\omega}_1, \boldsymbol{\omega}_2) = \left[1 - \frac{\chi}{2} \left(\frac{(\hat{\mathbf{r}}_{12} \cdot \boldsymbol{\omega}_1 + \hat{\mathbf{r}}_{12} \cdot \boldsymbol{\omega}_2)^2}{1 + \chi \boldsymbol{\omega}_1 \cdot \boldsymbol{\omega}_2} + \frac{(\hat{\mathbf{r}}_{12} \cdot \boldsymbol{\omega}_1 - \hat{\mathbf{r}}_{12} \cdot \boldsymbol{\omega}_2)^2}{1 - \chi \boldsymbol{\omega}_1 \cdot \boldsymbol{\omega}_2} \right) \right]^{-\frac{1}{2}}, \tag{3}$$

$$\begin{aligned} \epsilon(\hat{\mathbf{r}}_{12}, \boldsymbol{\omega}_1, \boldsymbol{\omega}_2) &= \epsilon_0 \left(1 - \chi^2 (\boldsymbol{\omega}_1 \cdot \boldsymbol{\omega}_2)^2 \right)^{-\frac{1}{2}} \\ &\times \left[1 - \frac{\chi'}{2} \left(\frac{(\hat{\mathbf{r}}_{12} \cdot \boldsymbol{\omega}_1 + \hat{\mathbf{r}}_{12} \cdot \boldsymbol{\omega}_2)^2}{1 + \chi' \boldsymbol{\omega}_1 \cdot \boldsymbol{\omega}_2} + \frac{(\hat{\mathbf{r}}_{12} \cdot \boldsymbol{\omega}_1 - \hat{\mathbf{r}}_{12} \cdot \boldsymbol{\omega}_2)^2}{1 - \chi' \boldsymbol{\omega}_1 \cdot \boldsymbol{\omega}_2} \right) \right]^2 . \end{aligned} \tag{4}$$

Here $\chi = (\kappa^2 - 1)/(\kappa^2 + 1)$ and $\kappa = L/R$, where R is the cross-sectional diameter of the particle and L is the particle length along the main symmetry axis (see Fig. 1). Accordingly, the parameter κ is a measure of the length-to-breadth ratio of the particle. The interaction strength $\epsilon(\hat{\mathbf{r}}_{12}, \boldsymbol{\omega}_1, \boldsymbol{\omega}_2)$ depends on the relative orientations of the particles, ϵ_0 is a parameter setting the energy scale of the pair interaction, $\chi' = (\kappa'^{1/2} - 1)/(\kappa'^{1/2} + 1)$, and $\kappa' = \epsilon_R/\epsilon_L$. Here ϵ_R is the minimum of the potential for a pair of parallel particles placed side-by-side ($\hat{\mathbf{r}}_{12} \cdot \boldsymbol{\omega}_1 = \hat{\mathbf{r}}_{12} \cdot \boldsymbol{\omega}_2 = 0$) and ϵ_L is

the minimum for a pair of parallel particles placed end-to-end ($\hat{\mathbf{r}}_{12} \cdot \boldsymbol{\omega}_1 = \hat{\mathbf{r}}_{12} \cdot \boldsymbol{\omega}_2 = 1$). The pair interaction potential due to the charges is decomposed into three terms

$$U_{CO}(\mathbf{r}_{12}, \boldsymbol{\omega}_1, \boldsymbol{\omega}_2) = U_{cc}(\mathbf{r}_{12}) + U_{ct}(\mathbf{r}_{12}, \boldsymbol{\omega}_1, \boldsymbol{\omega}_2) + U_{tt}(\mathbf{r}_{12}, \boldsymbol{\omega}_1, \boldsymbol{\omega}_2), \tag{5}$$

with

$$U_{cc}(\mathbf{r}_{12}) = \gamma_{cc} \frac{e^{-r_{12}/\lambda_D}}{r_{12}}, \tag{6}$$

$$U_{ct}(\mathbf{r}_{12}, \boldsymbol{\omega}_1, \boldsymbol{\omega}_2) = \gamma_{ct} \left[\frac{e^{-r_{c+}/\lambda_D}}{r_{c+}} + \frac{e^{-r_{+c}/\lambda_D}}{r_{+c}} + \frac{e^{-r_{c-}/\lambda_D}}{r_{c-}} + \frac{e^{-r_{-c}/\lambda_D}}{r_{-c}} \right], \tag{7}$$

$$U_{tt}(\mathbf{r}_{12}, \boldsymbol{\omega}_1, \boldsymbol{\omega}_2) = \gamma_{tt} \left[\frac{e^{-r_{++}/\lambda_D}}{r_{++}} + \frac{e^{-r_{+-}/\lambda_D}}{r_{+-}} + \frac{e^{-r_{-+}/\lambda_D}}{r_{-+}} + \frac{e^{-r_{--}/\lambda_D}}{r_{--}} \right]. \tag{8}$$

Here the distances between the charges are given by

$$r_{c\pm} = |\mathbf{r}_{12} \mp \boldsymbol{\omega}_2 D|, \qquad r_{\pm c} = |\mathbf{r}_{12} \pm \boldsymbol{\omega}_1 D|, \qquad r_{\pm\pm} = |\mathbf{r}_{12} \pm \boldsymbol{\omega}_1 D \mp \boldsymbol{\omega}_2 D|, \tag{9}$$

where D is distance between the center of the particle and the charges at the tails of the particle (see Fig. 1). The Debye screening length is denoted as λ_D and $\gamma_{cc} = z_c z_c e^2 / \varepsilon$, $\gamma_{ct} = z_c z_t e^2 / \varepsilon$, $\gamma_{tt} = z_t z_t e^2 / \varepsilon$ characterize the energy scale. Here the sites at the center and the tails of the particle carry the charges $z_c e$ and $z_t e$, respectively. The permittivity is denoted as ε. Any counterions will be considered at the linear response level, e.g., they will screen the electrostatic potential on a scale given by the Debye screening length.

B. Density functional theory

The number density of the center of mass of a particle at a point $\mathbf{r}$ with an orientation $\boldsymbol{\omega}$ is written as $\rho(\mathbf{r}, \boldsymbol{\omega}) = \rho f(\mathbf{r}, \boldsymbol{\omega})$, where $f(\mathbf{r}, \boldsymbol{\omega})$ represents a dimensionless distribution function and $\rho = N/V$ is the total number density. Here N is the number of particles and V is volume. The equilibrium density profile minimizes the grand potential functional (see, e.g., Refs.[27–31] and references therein):

$$\Omega[\{f(\mathbf{r}, \boldsymbol{\omega})\}, \rho, T, \mu] = k_B T \rho \left(\ln(4\pi\Lambda^3 \rho) - 1 \right) V + F[\{f(\mathbf{r}, \boldsymbol{\omega})\}, \rho, T] - \mu\rho V, \tag{10}$$

where μ is the chemical potential and Λ is the thermal de Broglie wavelength. The excess (over the ideal gas) free energy functional $F[\{f(\mathbf{r}, \boldsymbol{\omega})\}, \rho, T]$ is in general a very complicated, highly non-trivial object, because it is a characterizing property of a many-body problem. $F[\{f(\mathbf{r}, \boldsymbol{\omega})\}, \rho, T]$ is dealt with in various ways, which specify the explicit forms of the theory. We use the Parsons and Lee approach[32,33] for the hard core interaction together with a perturbation expansion for the long-ranged interaction:

$$F[\{f(\mathbf{r}, \boldsymbol{\omega})\}, \rho, T] = k_B T \rho \int d\mathbf{r}_1 \, d\boldsymbol{\omega}_1 \, f(\mathbf{r}_1, \boldsymbol{\omega}_1) \ln\left(f(\mathbf{r}_1, \boldsymbol{\omega}_1)\right)$$

$$+ \frac{\rho}{2} \int d\mathbf{r}_1 \, d\boldsymbol{\omega}_1 \, f(\mathbf{r}_1, \boldsymbol{\omega}_1) \left(U_{ref}[\{f(\mathbf{r}, \boldsymbol{\omega})\}, \rho, T] + U_{exc}[\{f(\mathbf{r}, \boldsymbol{\omega})\}, \rho, T]\right), \tag{11}$$

with

$$U_{ref}[\{f(\mathbf{r}, \boldsymbol{\omega})\}, \rho, T] = -k_B T J(\rho) \int d\mathbf{r}_2 \, d\boldsymbol{\omega}_2 \, f_M(\mathbf{r}_{12}, \boldsymbol{\omega}_1, \boldsymbol{\omega}_2) f(\mathbf{r}_2, \boldsymbol{\omega}_2), \tag{12}$$

$$U_{exc}[\{f(\mathbf{r}, \boldsymbol{\omega})\}, \rho, T] = \rho \int d\mathbf{r}_2 \, d\boldsymbol{\omega}_2 \, (1 - f_M(\mathbf{r}_{12}, \boldsymbol{\omega}_1, \boldsymbol{\omega}_2)) \, U(\mathbf{r}_{12}, \boldsymbol{\omega}_1, \boldsymbol{\omega}_2) f(\mathbf{r}_2, \boldsymbol{\omega}_2). \tag{13}$$

Here $f_M(\mathbf{r}_{12}, \boldsymbol{\omega}_1, \boldsymbol{\omega}_2)$ is the Mayer function of the hard core pair interaction potential between two particles. The Mayer function equals -1 if the particles overlap, i.e., $r_{12} < R\sigma(\hat{\mathbf{r}}_{12}, \boldsymbol{\omega}_1, \boldsymbol{\omega}_2)$, and is zero otherwise. We note that the range parameter $R\sigma(\hat{\mathbf{r}}_{12}, \boldsymbol{\omega}_1, \boldsymbol{\omega}_2)$ given by Eq. (3) is, to a first approximation, the contact distance between two hard ellipsoids of elongation κ with orientations $\boldsymbol{\omega}_1$ and $\boldsymbol{\omega}_2$ (see Ref.[34]). $U_{ref}[\{f(\mathbf{r}, \boldsymbol{\omega})\}, \rho, T]$ and $U_{exc}[\{f(\mathbf{r}, \boldsymbol{\omega})\}, \rho, T]$ are the effective reference and excess potential, respectively, acting on a particle due to the presence of the remaining

particles. The Parsons-Lee modification amounts to scaling the reference Onsager free energy functional by the function (see Eq. (12))

$$J(\rho) = \frac{1}{V_p} \frac{4\eta - 3\eta^2}{4(1-\eta)^2} \tag{14}$$

which incorporates the contributions of many-body hard core interactions in an approximate way. Here $\eta = \rho V_p$ and $V_p = \pi L R^2/6$ are the volume fraction and the particle volume, respectively. In the case of $J(\rho) = \rho$ the effective reference potential $U_{ref}[\{f(\mathbf{r}, \boldsymbol{\omega})\}, \rho, T]$ reduces to the original second-virial Onsager theory. The Parsons-Lee approach for thermodynamic properties of the isotropic and nematic phases of fluids consisting of hard ellipsoids or spherocylinders has been found to be in agreement with simulation data.[35–38]

The equilibrium distribution function $f(\mathbf{r}, \boldsymbol{\omega})$ is obtained from the extremum condition through the variation of the excess free energy functional with respect to $f(\mathbf{r}, \boldsymbol{\omega})$:

$$f(\mathbf{r}, \boldsymbol{\omega}) = \frac{1}{Z[\{f(\mathbf{r}, \boldsymbol{\omega})\}, \rho, T]} \exp\left(-\frac{U_{ref}[\{f(\mathbf{r}, \boldsymbol{\omega})\}, \rho, T]}{k_B T} - \frac{U_{exc}[\{f(\mathbf{r}, \boldsymbol{\omega})\}, \rho, T]}{k_B T}\right), \tag{15}$$

where the partition function is given by

$$Z[\{f(\mathbf{r}, \boldsymbol{\omega})\}, \rho, T] = \frac{1}{V} \int d\mathbf{r}\, d\boldsymbol{\omega}\, \exp\left(-\frac{U_{ref}[\{f(\mathbf{r}, \boldsymbol{\omega})\}, \rho, T]}{k_B T} - \frac{U_{exc}[\{f(\mathbf{r}, \boldsymbol{\omega})\}, \rho, T]}{k_B T}\right). \tag{16}$$

By substituting the distribution function $f(\mathbf{r}, \boldsymbol{\omega})$ back into the Eq. (11) the excess free energy functional can be written as

$$
\begin{aligned}
F[\{f(\mathbf{r}, \boldsymbol{\omega})\}, \rho, T]V^{-1} =\ & -k_B T \rho \ln\left(Z[\{f(\mathbf{r}, \boldsymbol{\omega})\}, \rho, T]\right) - \frac{\rho}{2} \langle U_{ref}[\{f(\mathbf{r}, \boldsymbol{\omega})\}, \rho, T]\rangle \\
& - \frac{\rho}{2} \langle U_{exc}[\{f(\mathbf{r}, \boldsymbol{\omega})\}, \rho, T]\rangle,
\end{aligned} \tag{17}
$$

where the average of a general functional of the distribution function $A[\{f(\mathbf{r}, \boldsymbol{\omega})\}]$ is

$$\langle A[\{f(\mathbf{r}, \boldsymbol{\omega})\}]\rangle = \frac{1}{V} \int d\mathbf{r}\, d\boldsymbol{\omega}\, f(\mathbf{r}, \boldsymbol{\omega}) A[\{f(\mathbf{r}, \boldsymbol{\omega})\}]. \tag{18}$$

Minimization of $\Omega[\{f(\mathbf{r}, \boldsymbol{\omega})\}, \rho, T, \mu]$ with respect to ρ leads to the following Euler-Lagrange equation for the density

$$\rho = \frac{e^{\mu/(k_B T)} Z[\{f(\mathbf{r}, \boldsymbol{\omega})\}, \rho, T]}{4\pi\Lambda^3} \exp\left(-\frac{\langle U_{ref}[\{f(\mathbf{r}, \boldsymbol{\omega})\}, \rho, T]\rangle}{2J(\rho)k_B T}\left(\rho\partial_\rho J(\rho) - J(\rho)\right)\right). \tag{19}$$

This equation can be solved numerically for a given chemical potential μ. The equation of state derived form the grand potential functional takes the following form:

$$
\begin{aligned}
P =\ & -\Omega[\{f(\mathbf{r}, \boldsymbol{\omega})\}, \rho, T, \mu]V^{-1} \tag{20} \\
=\ & \rho k_B T + \frac{\rho}{2}\left(\langle U_{exc}[\{f(\mathbf{r}, \boldsymbol{\omega})\}, \rho, T]\rangle + \frac{\langle U_{ref}[\{f(\mathbf{r}, \boldsymbol{\omega})\}, \rho, T]\rangle}{J(\rho)}\rho\partial_\rho J(\rho)\right). \tag{21}
\end{aligned}
$$

The densities, distribution functions, and thermodynamic properties of two coexisting phases I and II are found by solving the coexistence conditions $\mu_I = \mu_{II}$ and $P_I = P_{II}$ for a given temperature. Here μ_I, μ_{II} and P_I, P_{II} are the chemical potentials and the pressures of the coexisting phases, respectively.

C. Harmonic expansion

The effective reference and excess potentials are assumed to be of the general form

$$
\begin{aligned}
U_{ref}[S_2, W_0, W_2, d, \rho, T] \;=\; & \frac{J(\rho)}{2}\left(w_{00}^{(ref)}(\infty, T) + w_{22}^{(ref)}(\infty, T)P_2(\cos\theta)S_2\right) \\
& + \; J(\rho)\cos\left(2\pi z d^{-1}\right)\left(w_{00}^{(ref)}(d, T)W_0\right. \\
& + \; \left. w_{02}^{(ref)}(d, T)\left(W_2 + P_2(\cos\theta)W_0\right) + w_{22}^{(ref)}(d, T)P_2(\cos\theta)W_2\right),
\end{aligned}
\tag{22}
$$

$$
\begin{aligned}
U_{exc}[S_2, W_0, W_2, d, \rho, T] \;=\; & \frac{\rho}{2}\left(w_{00}^{(exc)}(\infty) + w_{22}^{(exc)}(\infty)P_2(\cos\theta)S_2\right) \\
& + \; \rho\cos\left(2\pi z d^{-1}\right)\left(w_{00}^{(exc)}(d)W_0 + w_{02}^{(exc)}(d)\left(W_2 + P_2(\cos\theta)W_0\right)\right. \\
& + \; \left. +w_{22}^{(exc)}(d)P_2(\cos\theta)W_2\right),
\end{aligned}
\tag{23}
$$

where $P_2(\cos\theta) = (3\cos^2\theta - 1)/2$ is the second Legendre polynomial and d is the layer spacing along z axis in the case of a smectic A phase. The order parameters S_2, W_0, and W_2 are given by

$$
S_2 = \langle P_2(\cos\theta)\rangle, \qquad W_0 = \left\langle \cos\left(2\pi z d^{-1}\right)\right\rangle, \qquad W_2 = \left\langle P_2(\cos\theta)\cos\left(2\pi z d^{-1}\right)\right\rangle.
\tag{24}
$$

The expansion coefficients $w_{ln}^{(ref)}(d, T)$ and $w_{ln}^{(exc)}(d)$ with $ln \in \{00, 02, 22\}$ are evaluated numerically according to

$$
\begin{aligned}
w_{ln}^{(ref)}(d, T) \;=\; & k_B T \int_0^\pi d\theta_1 \sin\theta_1 \int_0^\pi d\theta_2 \sin\theta_2 \int_0^{2\pi} d\phi \int d\mathbf{r}_{12}\, \Theta\left(R\,\sigma(\mathbf{r}_{12}, \boldsymbol{\omega}_1, \boldsymbol{\omega}_2) - \mathbf{r}_{12}\right) \\
& \times \; \cos\left(2\pi z_{12} d^{-1}\right) Q_{ln}(\boldsymbol{\omega}_1, \boldsymbol{\omega}_2),
\end{aligned}
\tag{25}
$$

$$
\begin{aligned}
w_{ln}^{(exc)}(d) \;=\; & \int_0^\pi d\theta_1 \sin\theta_1 \int_0^\pi d\theta_2 \sin\theta_2 \int_0^{2\pi} d\phi \int d\mathbf{r}_{12}\, \Theta\left(\mathbf{r}_{12} - R\,\sigma(\mathbf{r}_{12}, \boldsymbol{\omega}_1, \boldsymbol{\omega}_2)\right) \\
& \times \; U(\mathbf{r}_{12}, \boldsymbol{\omega}_1, \boldsymbol{\omega}_2)\cos\left(2\pi z_{12} d^{-1}\right) Q_{ln}(\boldsymbol{\omega}_1, \boldsymbol{\omega}_2)
\end{aligned}
\tag{26}
$$

with

$$
Q_{00}(\boldsymbol{\omega}_1, \boldsymbol{\omega}_2) = \frac{1}{4\pi}, \qquad Q_{02}(\boldsymbol{\omega}_1, \boldsymbol{\omega}_2) = \frac{5}{4\pi}\left(\frac{3}{2}\cos^2\theta_1 - \frac{1}{2}\right),
\tag{27}
$$

$$
Q_{22}(\boldsymbol{\omega}_1, \boldsymbol{\omega}_2) = \frac{25}{4\pi}\left(\frac{3}{2}\cos^2\theta_1 - \frac{1}{2}\right)\left(\frac{3}{2}\cos^2\theta_2 - \frac{1}{2}\right).
\tag{28}
$$

Here $\Theta(z)$ is the Heaviside step function and $\mathbf{r}_{12} = (x_{12}, y_{12}, z_{12})$. Equations (22) and (23) represent the first terms of an expansion of the effective reference and excess potentials in terms of spherical invariants (see, e.g., Refs.[39,40] and references therein).

The order parameters S_2, W_0, and W_2 in Eq. (24) serve to distinguish isotropic ($S_2 = W_0 = W_2 = 0$), nematic ($S_2 \neq 0$ and $W_0 = W_2 = 0$), and smectic A ($S_2, W_0, W_2 \neq 0$) phases. By introducing further order parameters it is possible to describe other liquid crystalline and crystalline structures. However, some of these additional phases are strongly non-uniform and they occur at high packing fractions, such that they are not expected to be well described by our approach and we therefore restrict ourselves to the three order parameters given in Eq. (24).

III. RESULTS

In this section we discuss fluid phase equilibria for nonspherical particles with the intermolecular pair potential given by Eq. (1). The phase diagrams have been calculated using the formalism presented in the previous section. In particular, the harmonic expansions of the effective reference and excess potentials [Eqs. (22) and (23)] have been

used as input into the expressions for the equilibrium distribution function [Eq. (15)] and the pressure [Eq. (21)]. It is convenient to examine the phase behavior in terms of the reduced temperature $T^\star = k_B T/\epsilon_0$, the packing fraction $\eta = \rho V_p$, the dimensionless strengths of the Coulomb interactions $E_{cc} = \gamma_{cc}/(\epsilon_0 R)$, $E_{ct} = \gamma_{ct}/(\epsilon_0 R)$, $E_{tt} = \gamma_{tt}/(\epsilon_0 R)$, and the reduced Debye screening length $\lambda_D^\star = \lambda_D/R$.

A. Influence of Gay-Berne potential and charges on the phase behavior

First we study the phase behavior of uncharged particles with the length-to-breadth ratio $\kappa = L/R = 2$ and the anisotropy parameter $\kappa' = 2$ of the Gay-Berne potential (solid lines in Figs. 2 (a) - (c)). The fluid is positionally and orientationally disordered ($S_2 = W_0 = W_2 = 0$) in the isotropic phase (I) at low packing fractions η and high enough temperatures $T^\star$. Upon increasing the packing fraction, a first-order phase transition to a smectic A phase (S$_A$) with $S_2, W_0, W_2 \neq 0$ occurs. The isotropic fluid undergoes a vapor-liquid separation below the critical temperature $T_c^\star$ marked by the solid circles in Figs. 2 (a) - (c). Upon increasing the packing fraction, the phase sequence is vapor (V), isotropic liquid, and smectic A for temperatures $T_t^\star < T^\star < T_c^\star$. Here $T_t^\star$ is the triple point temperature (thin solid line in Figs. 2 (a) - (c)) at which the three phases V, I, and S_A coexist. Increasing the anisotropy parameter κ' of the Gay-Berne potential at fixed κ leads to a shift of the vapor-liquid coexistence curve to lower temperatures as is apparent from Fig. 2 (a) where the phase diagram is shown for $\kappa' = 2$ (solid line) and $\kappa' = 5$ (dotted line). Moreover, the smectic region is pushed to lower packing fractions as κ' increases. High values of κ' favor the side-by-side configuration over the end-to-end configuration of two parallel particles. Therefore, the packing fractions of the coexisting isotropic and smectic A phases decrease upon increasing κ'. The relative stability of the side-by-side configuration decreases as κ' is lowered and for $\kappa' = 1$ all configurations are equally stable for parallel particles, i.e., $\epsilon(\mathbf{r}_{12}, \boldsymbol{\omega}_1, \boldsymbol{\omega}_2) = \epsilon_0$ for $\kappa' = 1$ and $\boldsymbol{\omega}_1 \parallel \boldsymbol{\omega}_2$ in Eq. (4).

Figure 2 (b) demonstrates that the width of the I-S_A phase transition broadens upon increasing the length-to-breadth ratio of the particles from $\kappa = L/R = 2$ (solid line) to $\kappa = 4$ (dash-dotted line). Furthermore, the vapor-liquid coexistence curve is metastable with respect to the I-S_A coexistence for $\kappa = 4$. More details concerning the influence of the length-to-breadth ratio of the particles and the anisotropy parameter of the Gay-Berne potential on the fluid phase behavior can be found in Refs.[23,24].

We examine now the influence of two like charges ($E_{tt} = 45, \lambda_D^\star = 50$) located at the tails ($D/R = 0.9$ for $\kappa = D/R = 2$, see Fig. 1) on the fluid phase behavior (dashed line in Fig. 2 (c)). The vapor-liquid critical temperature is seen to decrease with increasing the Coulomb interaction strength and the I-S_A coexistence region is shifted to higher packing fractions. In the high-temperature limit the thermodynamic properties of the fluid are dominated by the repulsive steric interactions, and the I-S_A phase transition tends to that of the corresponding hard core fluid, with packing fractions $\eta_I = 0.61$ and $\eta_{S_A} = 0.63$ at I-S_A phase coexistence. The decrease of the vapor-liquid critical temperature is due to the repulsive Coulomb pair interaction between the like charged tails of the particles.

B. Influence of the location of charges on the phase behavior

The effect of varying the location of charges on the particles with a fixed length-to-breadth ratio $L/R = 3$ and at a fixed temperature $T^\star = 1.5$ is now examined. Fluid phases are shown in Fig. 3 as functions of the strength of the Coulomb pair interactions E_{tt} or E_{cc}, and the packing fraction η for three different locations of the charges. Two like charges are located at the distance $D = 1.4R$ and $D = R$ from the center of the particles in Fig. 3 (a) and (b), respectively, while a single charge is located at the center of the particles in Fig. 3 (c). The length-to-breadth ratio and temperature have been chosen such that the fluids consisting of uncharged particles (i.e., $E_{tt} = E_{cc} = 0$) are isotropic at low packing fractions and a phase transition to the smectic A phase is observed at higher packing fractions. There is an important difference between the phase behavior of fluids consisting of particles with charges located at $D = 1.4R$ and at $D = R$. While for $D = R$ the smectic A phase is the only stable phase at high packing fractions (see Fig. 3 (b)), nematic phase ordering (N) with $S_2 \neq 0$ and $W_0 = W_2 = 0$ is found for $D = 1.4R$ (see Fig. 3 (a)). In this case the nematic phase is stable for strong Coulomb pair interaction down to $E_{tt} = 215$ at the I-N-S_A triple point. In the case of particles with two like charges located at the distance $D = R$ from the center, there is no stable nematic phase even at higher Coulomb interaction strengths. In this case the packing fractions of the coexisting isotropic and smectic A phases (solid lines in Fig. 3 (b)) decrease with increasing Coulomb interaction strength E_{tt}, whereas the packing fractions of the metastable isotropic-nematic phase coexistence (dashed lines in Fig. 3 (b)) increase.

Surprisingly, the nematic phase is stable in the case of a fluid consisting of particles with a single charge located at the center as is shown in Fig. 3 (c). The smectic A phase is preempted by the nematic phase which is stable above the Coulomb interaction strength $E_{cc} = 10465$ at the I-N-S_A triple point.
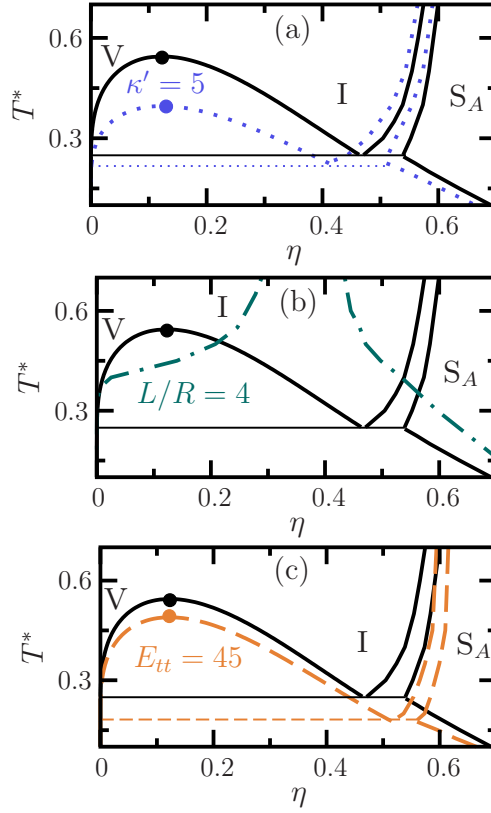
FIG. 2: The influence of the anisotropy parameter of the Gay-Berne potential κ' in panel (a), the length-to-breadth ratio of the particles $\kappa = L/R$ in panel (b), and like charges at the tails of the particles in panel (c) on the fluid phase behavior of an ionic liquid crystal consisting of ellipsoidal particles (see Fig. 1). The phase diagrams are shown as functions of the packing fraction η and the reduced temperature $T^\star$. The solid lines in panels (a), (b), and (c) represent the phase diagram for uncharged particles with $\kappa = 2$ and $\kappa' = 2$, while the dotted and dash-dotted lines show the phase diagram for uncharged particles with $\kappa = 2$, $\kappa' = 5$ in panel (a) and $\kappa = 4$, $\kappa' = 2$ in panel (b). The dashed line in panel (c) represents the phase diagram for charged particles with $\kappa = 2$, $\kappa' = 2$, $D/R = 0.9$, $E_{tt} = 45$, and $\lambda_D^\star = 50$. The solid horizontal lines in panels (a), (b), and (c) mark the coexistence of a vapor phase (V) with an isotropic liquid phase (I) and a smectic phase A (S_A) for the uncharged particles with $\kappa = 2$ and $\kappa' = 2$, while the solid circles mark the vapor-liquid critical point. The lower circles in panels (a) and (c) denote the vapor-liquid critical points corresponding to the phase diagrams represented by the dotted and dashed lines, respectively. Vapor-liquid coexistence is metastable for the length-to-breadth ratio $\kappa = 4$ in panel (b). The dashed horizontal line in panel (c) corresponds to V-I-S_A three phase coexistence of the fluid consisting of charged particles.

In order to understand the influence of the location of two like charges on the fluid phase behavior it is instructive to consider a set of position-dependent order parameters which quantifies the deviation of the number density from isotropy.[41] The normalized, orientationally averaged density profile

$$n(z) = 2\pi \int_0^\pi d\theta \, \sin\theta \, f(z,\theta) \tag{29}$$

and the position-dependent, relative nematic order parameter

$$s(z) = \frac{\pi}{n(z)} \int_0^\pi d\theta \, \sin\theta \, (3\cos^2\theta - 1) f(z,\theta) \tag{30}$$

are displayed in Fig. 4 (a) and (b), respectively. The solid lines show the profiles for particles with two like charges located at the distance $D = R$ from the center of the particles (see Fig. 3 (b)), while the dashed lines display the profiles for particles with a single charge located at the center of the particles (see Fig. 3 (c)). The packing fraction is fixed to $\eta = 0.67$ and the Coulomb pair interaction strengths are given by $E_{tt} = E_{cc}/4 = 4000$. Hence the smectic A
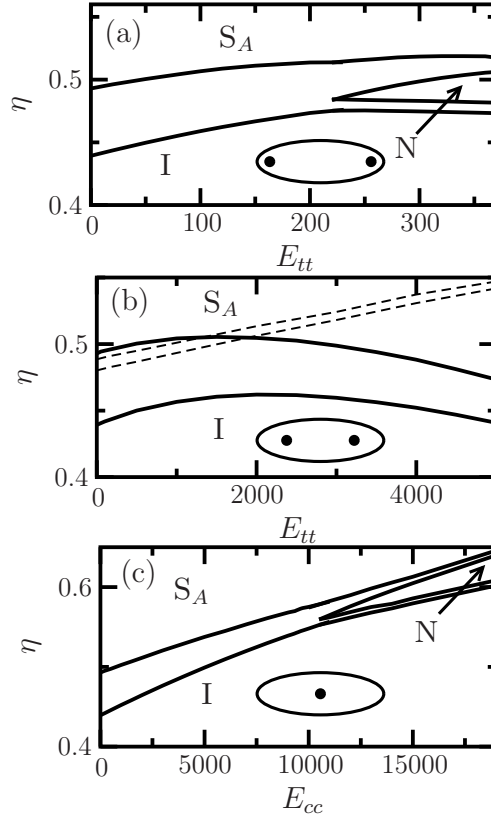
FIG. 3: The influence of the location of two like charges on the fluid phase behavior of an ionic liquid crystal consisting of charged ellipsoidal particles with length-to-breadth ratio $\kappa = L/R = 3$ at temperature $T^\star = 1.5$. The anisotropy parameter of the Gay-Berne potential and the Debye screening length are fixed to $\kappa' = 8$ and $\lambda_D^\star = 50$, respectively. Two like charges are located at the distance $D = 1.4R$ and $D = R$ from the center of the particles in panels (a) and (b), respectively, while a single charge is located at the center of the particles in panel (c). Schematic illustrations of the shape of the particles and the location of the charges (solid dots) are shown in the figures. The phase diagrams are plotted as functions of the Coulomb pair interaction strengths E_{tt} or E_{cc}, and the packing fraction η. The solid lines denote the phase boundaries of thermal equilibrium of an isotropic (I), nematic (N), and smectic A (S_A) phase, while the dashed lines in panel (b) mark metastable isotropic-nematic phase coexistence.

phase is stable and the particles in panels (a) and (b) carry the same total charge. The order parameter profiles are periodic functions with layer spacings $d \approx 3.8R$ and $d \approx 3.0R$ for the particles with two like charges at the tails (solid lines) and the particles with a single charge located at the center (dashed lines), respectively. The density profiles of the centers of the particles exhibit maxima in the center of the layers at $z = 0$ as is apparent from Fig. 4 (a). Moreover, the density distribution along the layer axis is sharper for the particles with two like charges at the tails than that for the particles with a single charge located at the center.

Figure 4 (b) demonstrates that there is a qualitative difference between the relative nematic order parameter profiles for particles with two like charges at the tails (solid lines) and the particles with a single charge located at the center (dashed lines). Whereas $s(z)$ is rather independent of z in the latter case, the relative nematic order parameter profile exhibits pronounced oscillations along the z axis in the former case, where particles located between the layers at $|z/d| \gtrsim 0.4$ are oriented with their main body mainly perpendicular to the z axis, i.e., $s(z) < 0$. For comparison we recall that the value of the nematic order parameter is $s(z) = -0.5$ and $s(z) = 1.0$ for perfect perpendicular and parallel alignment to the z axis, respectively. The predominantly perpendicular orientation of particles with charges at the tails located in between the smectic layers can be understood in terms of a minimization of the electrostatic repulsion due to a maximized distance from the particles in the smectic layers. For particles with the charge in the center the electrostatic energy is independent of the orientation; hence a parallel alignment of particles in between smectic layers is favourable, as non-parallel orientations would increase the free energy due to an increase in the layer spacing. The latter case is comparable with the results of van Roij et al.[42] on uncharged spherocylinders (see Fig. 2 of Ref.[42]), where the majority of inter-layer particles is aligned parallel to the layer normal. The bimodal orientational
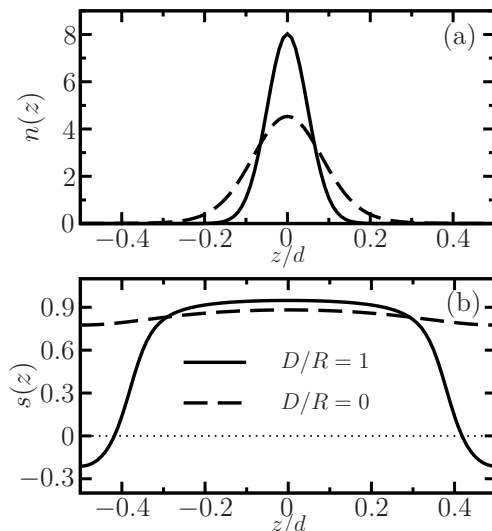
FIG. 4: Normalized, orientationally averaged density profile $n(z)$ [Eq. (29)] in panel (a) and relative nematic order parameter $s(z)$ [Eq. (30)] in panel (b) of an ionic liquid crystal along the z-axis in the smectic A phase, where d is the layer spacing. The solid lines represent the profiles for particles with two like charges located at the distance $D = R$ from the center of the particles (see Fig. 3 (b)), while the dashed lines show the profiles for particles with a single charge located at the center of the particles (see Fig. 3 (c)). The model parameters are fixed to $\kappa = L/R = 3$, $\kappa' = 8$, $T^\star = 1.5$, $\eta = 0.67$, and $E_{tt} = E_{cc}/4 = 4000$. Therefore, the particles in panels (a) and (b) carry the same total charge.

distribution described in Ref.[42] is also expected to be found in the present situation.

C. Influence of the particle length on the phase behavior

We now study the effect of varying the length-to-breadth ratio $\kappa = L/R$ for charged particles with two like charges located at a fixed distance $L/2 - D = 0.1R$ from the end of the particles (see Fig. 1). Fluid phases are shown in Fig. 5 as functions of the strength of the Coulomb pair interaction E_{tt} and the packing fraction η for a fixed temperature $T^\star = 2$. The length-to-breadth ratio is $\kappa = 3$ and $\kappa = 5$ in Fig. 5 (a) and (b), respectively. Qualitatively similar types of phase behavior are exhibited by both systems. The fluids consisting of uncharged particles, i.e., $E_{tt} = 0$, are isotropic at low packing fractions and a phase transition to the smectic A phase is observed at higher packing fractions. Upon increasing the Coulomb pair interaction strength E_{tt} stable nematic islands in the phase diagrams are found. This nematic phase is bounded below and above by isotropic and smectic A phases, respectively. Moreover, the location of the nematic region is seen to move to higher Coulomb pair interaction strength and lower volume fraction upon increasing the length-to-breadth ratio. The nematic phase disappears at high values of the Coulomb pair interaction strength when the repulsive steric interaction is less important. The competition of the steric interaction and the Coulomb pair interaction leads to the existence of a stable nematic phase for intermediate values of E_{tt}. Moreover, we emphasize that the smectic A phase is stabilized for high Coulomb interaction strengths. Hence molecules which are not mesogenic without charges at a given packing fraction can form a stable smectic phase if they are charged at the same packing fraction. Furthermore, it is worthwhile to note that using larger Debye screening lengths leads to phase diagrams of the same topology as the ones presented in Fig. 5 (data not shown). However, the corresponding Coulomb interaction strengths are smaller due to the longer ranged interaction potential.

Packing fraction-temperature projections of the fluid phase diagrams for the systems with $E_{tt} = 300$ (see the dotted lines in Fig. 5) are shown in Fig. 6. The stable isotropic, nematic, and smectic A regions are clearly visible for the fluid consisting of the smaller particles in Fig. 6 (a). For the larger particles the isotropic-nematic coexistence region is metastable with respect to the I-S_A coexistence (dashed lines in Fig. 6 (b)). For both systems, the low temperature part of the phase diagram is dominated by a wide two-phase region where the S_A phase is in equilibrium with an isotropic phase. We note that the behavior is reverse for $E_{tt}^{(l)} > E_{tt} > E_{tt}^{(s)}$, where $E_{tt}^{(s)} = 1099$ and $E_{tt}^{(l)} = 1570$ is the second triple point for the smaller and larger particles, respectively (see Fig. 5 (a)). Increasing the length-to-breadth ratio induces the nematic phase in this case.

The model described in Sec. II A of ellipsoidal particles with point charges may be compared with models of
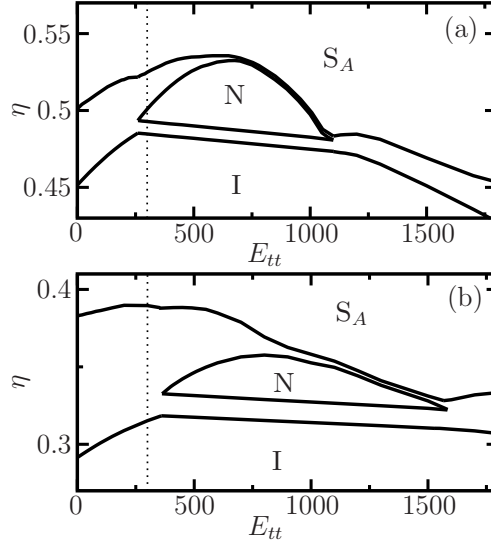
FIG. 5: The influence of the length-to-breadth ratio $\kappa = L/R$ on the fluid phase behavior of an ionic liquid crystal consisting of charged ellipsoidal particles with two like charges located at a fixed distance $L/2 - D = 0.1R$ from the end of the particles (see Fig. 1). The length-to-breadth ratio is $\kappa = 3$ in panel (a) and $\kappa = 5$ in panel (b). The anisotropy parameter of the Gay-Berne potential and the Debye screening length are fixed to $\kappa' = 8$ and $\lambda_D^\star = 50$, respectively. The phase diagrams are plotted as functions of the Coulomb pair interaction strength E_{tt} and the packing fraction η for the fixed temperature $T^\star = 2$. The solid lines denote the phase boundaries of thermal equilibrium of an isotropic (I), nematic (N), and smectic A (S_A) phase. In Fig. 6 phase diagrams are shown as functions of the packing fraction and the temperature for the Coulomb pair interaction strength indicated by the dotted lines.
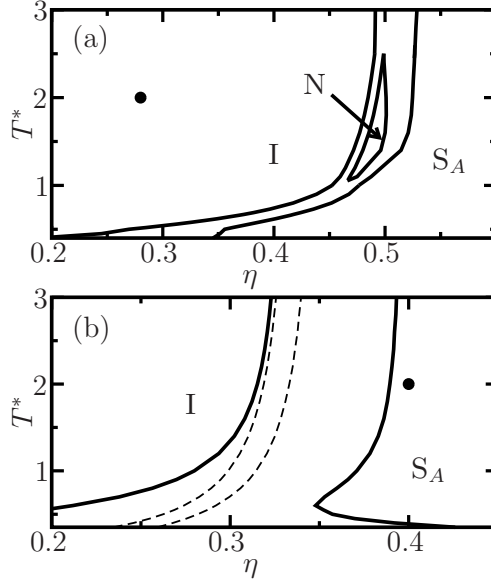

FIG. 6: Phase diagrams of the same fluids as in Fig. 5 in the packing fraction (η) - temperature ($T^\star$) plane. The Coulomb pair interaction strength is given by $E_{tt} = 300$ as indicated by the dotted lines in Fig. 5. The length-to-breadth ratio is $\kappa = 3$ in panel (a) and $\kappa = 5$ in panel (b). The solid lines denote the phase boundaries of thermal equilibrium of an isotropic (I), nematic (N), and smectic A (S_A) phase, while the dashed lines in panel (b) mark metastable isotropic-nematic phase coexistence. In panel (a) and (b) the solid circles denote two state points with equal temperature and pressure.

spherocylinders with line charges.[43–45] The presence of a direct isotropic-smectic transition for small length-to-breadth ratios $\kappa = L/R$ and charges E_{tt}, the decrease of the packing fraction at the transition upon increasing κ, as well as

the increase of the packing fraction at the transition upon increasing E_{tt} (see Fig. 5) are in agreement with the trends for spherocylinders as displayed in Figs. 2 and 3 of Ref.[44]. Hence there is qualitative similarity between our model of point charges at the particle tails and charged spherocylinders with line charges.

D. Varying the strength of the Coulomb interaction

We next consider the influence of the Coulomb interaction strength on the phase behavior. The locations of the various ordering transitions in the case of a fluid consisting of ellipsoidal particles with a single charge located in the center of the particles and the length-to-breadth $\kappa = 3$ are summarized in Fig. 7 for three different Coulomb interaction strengths E_{cc}. From the phase behavior of the systems shown in Fig. 7, it is apparent that the nematic phase becomes stable with increasing Coulomb interaction strength. There are I-N-S_A triple points for the Coulomb interaction strengths $E_{cc} = 4500$ and $E_{cc} = 15000$ in Figs. 7 (b) and (c), respectively, while the I-N coexistence region is metastable in the case of the weaker Coulomb interaction strength considered in Fig. 7 (a). In the high-temperature limit the thermodynamic properties of the fluids are dominated by the repulsive steric interactions, and the I-S_A phase transition tends to that of the corresponding hard core fluid. As expected the isotropic region becomes more extensive as the Coulomb interaction strength is increased. In the case of a large Coulomb interaction strength the long-ranged pair potential is rather independent of the orientations of the particles because the charges are located in the center of the ellipsoids. Therefore the locations of phase transitions from the isotropic phase to orientationally ordered phases in the low temperature region are shifted to higher packing fractions upon increasing the Coulomb interaction strength.
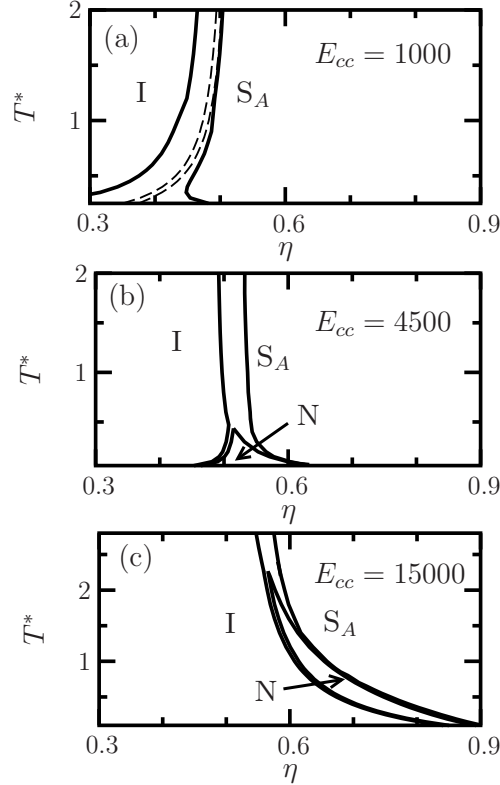

FIG. 7: The influence of the Coulomb pair interaction strength E_{cc} on the fluid phase behavior of an ionic liquid crystal consisting of ellipsoidal particles ($\kappa = L/R = 3$) with a single charge located in the center of each particle. The phase diagrams are shown as functions of the packing fraction η and the reduced temperature $T^\star$. The solid lines denote the phase boundaries of thermal equilibrium of an isotropic (I), nematic (N), and smectic A (S_A) phase, while the dashed lines in panel (a) mark metastable isotropic-nematic phase coexistence. The anisotropy parameter of the Gay-Berne potential and the Debye screening length are given by $\kappa' = 8$ and $\lambda_D^\star = 50$, respectively.

E.   Comparison with experimental results

In general the total number density of both thermotropic liquid crystals (see, e.g., Ref.[46]) and colloidal suspensions consisting of charged nonspherical particles (see, e.g., Ref.[47]) is smaller in the isotropic phase than in the coexisting nematic or smectic phase similar to our findings presented in Figs. 2, 3, and 5 - 7. Nevertheless, it is worthwhile to mention that the density of hard platelike particles in a binary mixture of thick and thin platelets can be larger in the isotropic phase than in the coexisting nematic phase depending on the chemical potentials.[48] This remarkable phenomenon of isotropic-nematic density inversion has been investigated using a two-component density functional theory for hard nonspherical particles.[49]

Hessel et al.[50] observed isotropic and smectic phases of molecules consisting of two pyridinium head groups and a biphenylene core (see Fig. 8 (a)). Increasing the length of the alkyl chains, i.e., increasing n in Fig. 8 (a), stabilizes the smectic phase. Both the transition temperature from the isotropic to the smectic phase and the layer spacing in the smectic phase increase with increasing length of the alkyl chains. These results agree with the theoretical results presented in Figs. 5 and 6. Increasing the length L of particles with two like charges located at a fixed distance $L/2 - D$ from the center of the particles (see Fig. 1) has a stabilizing effect on the smectic phase. For example, the isotropic phase is stable for particles with $\kappa = 3$ at the state point denoted by the solid circle in Fig. 6 (a), while the smectic A phase is s stable for larger particles with $\kappa = 5$ at the same temperature and pressure marked by the solid circle in Fig. 6 (b). Moreover, the calculated layer spacing d increases upon increasing L.
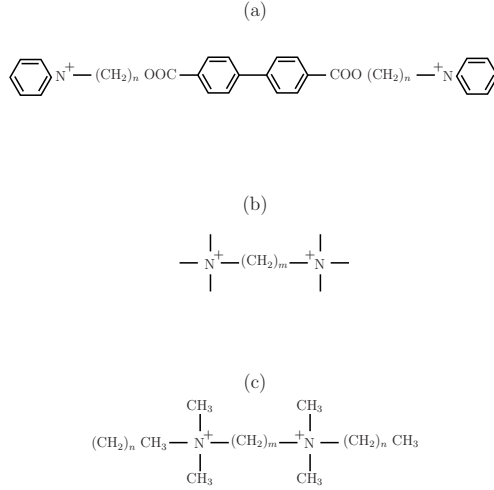

FIG. 8: Chemical structure of dipolar amphiphiles with two pyridinium head groups and a biphenylene core in (a), diquaternary ammonium salts in (b), and diammonium salts in (c). These molecules exhibit liquid crystalline phases.[50–52]

Kokkinia and Paleos[51] investigated the phase behavior of $\alpha - \omega$ diquaternary ammonium salts (see Fig. 8 (b)). By increasing the spacer length between the quaternary nitron atoms, more stable smectic phases were obtained in agreement with both the theoretical results shown in Figs. 5 and 6 as well as the aforementioned experimental study on dipolar amphiphiles with two pyridinium head groups and a biphenylene core.[50]

Thermotropic and lyotropic mesomorphism has been observed for the diammonium salts shown in Fig. 8 (c).[52] Interestingly, a stable nematic phase has been found for small spacer length $(CH_2)_m$. This nematic phase disappeared upon increasing the spacer length similar to our theoretical findings shown in Figs. 6 (a) and (b). Moreover, it is worthwhile to mention that a decrease of the layer spacing of the smectic phase with increasing temperature has been observed for various ionic liquid crystals[20] in agreement with the results of the present theoretical approach.

IV.   SUMMARY AND DISCUSSION

We have investigated bulk properties of ionic liquid crystals using density functional theory. The liquid crystal molecules are modeled as charged ellipsoids with cross-sectional diameter R and length L. Possible charges are located in the center of the particles or at the tails at a distance D from the center (see Fig. 1). The intermolecular pair potential is expressed as a sum of the contributions due to excluded-volume interactions and the contribution due to long-ranged interactions [Eq. (1)]. These long-ranged interactions are taken into account in terms of the Gay-Berne potential [Eqs. (2) - (4)] and the screened Coulomb interaction [Eqs. (5) - (9)]. The grand potential functional

[Eq. (10)] is minimized numerically and phase diagrams, density profiles, and orientational order parameter profiles are determined leading to the following main results:

(1) The phase diagrams for representative examples of liquid crystals involve a vapor, an isotropic liquid, and a smectic A phase (see Fig. 2). Increasing the anisotropy parameter of the Gay-Berne potential leads to a shift of the vapor-liquid coexistence curve to lower temperatures (see Fig. 2 (a)). The width of the isotropic to smectic phase transition broadens upon increasing the length-to-breadth ratio of the particles (see Fig. 2 (b)).

(2) There is a pronounced dependence of the phase behavior on the location of two like charges on the ellipsoidal particles (see Fig. 3). While for $D = R$ the smectic A phase is the only stable phase at high packing fractions (see Fig. 3 (b)), nematic phase ordering is found for $D = 1.4R$ (see Fig. 3 (a)). Moreover, the nematic phase is stable in the case of a fluid consisting of particles with a single charge located at the center (see Fig. 3 (c)). Whereas the relative nematic order parameter profile $s(z)$ is rather independent of z in the smectic A phase of particles with a single charge located at the center, it exhibits pronounced oscillations along the z axis in the case of two like charges at the tails at a distance $D = R$ from the center of the particles (see Fig. 4 (b)).

(3) Increasing the length L of the particles with two like charges located at a fixed distance $L/2 - D$ from the center of the particles has a stabilizing effect on the smectic A phase in agreement with earlier experimental findings (see Figs. 5 and 6). Moreover, the calculated layer spacing in the smectic A phase increases upon increasing the length L. With increasing the Coulomb pair interaction strength stable nematic islands in the phase diagrams are found (see Fig. 5). This nematic phase is bounded by isotropic and smectic A phases. Moreover, the location of the nematic region moves to higher Coulomb pair interaction strength and lower volume fraction upon increasing the length of the particles.

(4) For particles with a single charge located in the center, the isotropic region in the phase diagram becomes more extensive as the Coulomb interaction strength is increased (see Fig. 7) similar to earlier theoretical findings for charged platelike particles.[53] Moreover, a nematic phase becomes stable with increasing the Coulomb interaction strength (see Figs. 7 (b) and (c)). In the case of a large Coulomb interaction strength the long-ranged pair potential is rather independent of the orientations of the particles because the charges are located in the center of the ellipsoids.

Finally, we would like to emphasize that the methodology developed here can be extended to enable a quantitative treatment of the counterions by considering a multi-component density functional theory similar to earlier studies of nonspherical particles with charges located in the center.[53,54] A two-component model can be used to study the influence of the small ions on the liquid crystal molecules. On the basis of earlier multi-component integral equation studies it is known that the small ions screen the Coulomb interaction between the bigger particles in the liquid phase.[55–57] This justifies the use of a one-component model with the screened Coulomb interaction [Eqs. (5) - (9)]. But the two-component model may help to elucidate the influence of possible ionic clusters on the liquid-vapor coexistence of room-temperature ionic liquids.[58,59]

---

* E-mail: harnau@fluids.mpi-stuttgart.mpg.de

[1] D. Adam, P. Schuhmacher, J. Simmerer, L. Häussling, K. Siemensmeyer, K. H. Etzbach, H. Ringsdorf, and D. Haarer, Nature **371**, 141 (1994).

[2] M. O'Neill and S. M. Kelly, Adv. Mater. **15**, 1135 (2003).

[3] T. Kato, Science **295**, 2414 (2002).

[4] M. Yoshio, T. Mukai, K. Kanie, M. Yoshizawa, H. Ohno, and T. Kato, Adv. Mater. **14**, 351 (2002).

[5] C. M. Gordon, J. D. Holbrey, A. R. Kennedy, and K. R. Seddon, J. Mater. Chem. **8**, 2627 (1998).

[6] A. E. Bradley, C. Hardacre, J. D. Holbrey, S. Johnston, S. E. J. McMath, and M. Nieuwenhuyzen, Chem. Mater. **14**, 629 (2002).

[7] K.-M. Lee, Y.-T. Lee, and I. J. B. Lin, J. Mater. Chem. **13**, 1079 (2003).

[8] J. De. Roche., C. M. Gordon, C. T. Imrie, M. D. Ingram, A. R. Kennedy, F. Lo Celso, and A. Triolo, Chem. Mater. **15**, 3089 (2003).

[9] D. Ster, U. Baumeister, J. Lorenzo Chao, C. Tschierske, and G. Israel, J. Mater. Chem. **17**, 3393 (2007).

[10] P. H. J. Kouwer and T. M. Swager, J. Am. Chem. Soc. **129**, 14042 (2007).

[11] J. D. Holbrey and K. R. Seddon, J. Chem. Soc. Dalton Trans. **13**, 2133 (1999).

[12] C. Hardacre, J. D. Holbrey, P. B. McCormac, S. E. J. McMath, M. Nieuwenhuyzen, and K. R. Seddon, J. Mater. Chem. **11**, 346 (2001).

[13] S. Sauer, S. Saliba, S. Tussetschläger, A. Baro, W. Frey, F. Giesselmann, S. Laschat, and W. Kantlehner, Liq. Cryst. **36**, 275 (2009).

[14] F. Neve, A. Crispini, S. Armentano, O. Francescangeli, Chem. Mater. **10**, 1904 (1998).

[15] F. Neve, O. Francescangeli, A. Crispini, J. Charmant, Chem. Mater. **13**, 2032 (2001).

[16] M. Yoshio, T. Mukai, H. Ohno, and T. Kato, J. Am. Chem. Soc. **126**, 994 (2004).

[17] A. Taubert, Angew. Chem. Int. Ed. **43**, 5380 (2004).

[18] A. Taubert, P. Steiner, and A. Mantion, J. Phys. Chem. B **109**, 15542 (2005).

[19] S. Sauer, N. Steinke, A. Baro, S. Laschat, F. Giesselmann, and W. Kantlehner, Chem. Mater. **20**, 1909 (2008).

[20] K. Binnemanns, Chem. Rev. **105**, 4148 (2005).

[21] J. G. Gay and B. J. Berne, J. Phys. Chem. **74**, 3316 (1981).

[22] E. de Miguel, L. F. Rull, M. K. Chalam, and K. E. Gubbins, Molec. Phys. **74**, 405 (1991).

[23] E. de Miguel, E. M. del Rio, J. T. Brown, and M. P. Allen, J. Phys. Chem. **105**, 4234 (1996).

[24] J. T. Brown, M. P. Allen, E. M. del Rio, and E. de Miguel, Phys. Rev. E **57**, 6685 (1998).

[25] M. A. Bates and G. R. Luckhurst, J. Phys. Chem. **110**, 7087 (1999).

[26] E. de Miguel and C. Vega, J. Phys. Chem. **117**, 6313 (2002).

[27] R. Evans in *Fundamentals of Inhomogeneous Fluids*, edited D. Henderson, p. 85, (Dekker, New York, 1992).

[28] L. Harnau and S. Dietrich, Phys. Rev. E **71**, 011504 (2005).

[29] L. Harnau and S. Dietrich in *Soft Matter*, edited by G. Gompper and M. Schick (Wiley-VCH, Berlin, 2007), Vol. 3, p. 159.

[30] J. Wu, AIChE Journal **52**, 1169 (2006).

[31] L. Harnau Mol. Phys. **106**, 1975 (2008).

[32] J. D. Parsons, Phys. Rev. A **19**, 1225 (1979).

[33] S. D. Lee, J. Chem. Phys. **87**, 4972 (1987).

[34] D. J. Cleaver, C. M. Care, M. P. Allen, and M. P. Neal, Phys. Rev. E **54**, 559 (1996).

[35] A. Samborski, G. T. Evans, C. P. Mason, and M. P. Allen, Molec. Phys. **81**, 263 (1994).

[36] P. J. Camp, C. P. Mason, M. P. Allen, A. A. Khare, and D. A. Kofke, J. Phys. Chem. **105**, 2837 (1996).

[37] S. C. McGrother, D. C. Williamson, and G. Jackson, J. Phys. Chem. **104**, 6755 (1996).

[38] M. Franco-Melgar, A. J. Haslam, and G. Jackson, Molec. Phys. **106**, 649 (2008).

[39] M. V. Gorkunov, F. Giesselmann, J. P. F. Lagerwall, T. J. Sluckin, and M. A. Osipov, Phys. Rev. E **75**, 060701(R) (2007).

[40] M. V. Gorkunov, M. A. Osipov, J. P. F. Lagerwall, and F. Giesselmann, Phys. Rev. E **76**, 051706 (2007).

[41] L. Harnau and S. Dietrich, Phys. Rev. E **65**, 021505 (2002).

[42] R. van Roij, P. Bolhuis, B. Mulder, and D. Frenkel, Phys. Rev. E **52**, 1277 (1995).

[43] H. Graf and H. Löwen, Phys. Rev. E **59**, 1932 (1999).

[44] E. M. Kramer and J. Herzfeld, Phys. Rev. E **61**, 6872 (2000).

[45] E. Eggen, M. Dijkstra, and R. van Roij, Phys. Rev. E **79**, 041401 (2009).

[46] E. McLaughlin, M. A. Shakespeare, and A. R. Ubbelohde, Trans. Faraday Soc. **60**, 25 (1964).

[47] Z. Dogic and S. Fraden, in *Soft Matter*, edited by G. Gompper and M. Schick (Wiley-VCH, Berlin, 2006), Vol. 2, p. 69.

[48] F. M. van der Kooij, D. van der Beek, and H. N. W. Lekkerkerker, J. Phys. Chem. B **105**, 1696 (2001).

[49] M. Bier, L. Harnau and S. Dietrich, Phys. Rev. E **69**, 021506 (2004).

[50] V. Hessel, H. Ringsdorf, R. Festag, and J. H. Wendorff, Makromol. Chem. Rapid Commun. **14**, 707 (1993).

[51] A. Kokkinia and C. M. Paleos, Mol. Cryst. Liq. Cryst. **186**, 239 (1990).

[52] S. Fuller, N. N. Shinde, and G. J. T. Tiddy, Langmuir **12**, 1117 (1996).

[53] M. Bier, L. Harnau and S. Dietrich, J. Chem. Phys. **123**, 114906 (2005).

[54] M. Bier, L. Harnau and S. Dietrich, J. Chem. Phys. **125**, 184704 (2006).

[55] L. Harnau and P. Reineker, J. Chem. Phys. **112**, 437 (2000).

[56] L. Harnau, D. Costa, and J.-P. Hansen, Europhys. Lett. **53**, 729 (2001).

[57] L. Harnau and J.-P. Hansen, J. Chem. Phys. **116**, 9051 (2002).

[58] L. P. N. Reblo, J. N. Canongia Lopes, J. M. S. S. Esperanca, and E. Filipe, J. Phys. Chem. B **109**, 6040 (2005).

[59] M. Martin-Betancourt, J. M. Romero-Enrique, and L. F. Rull, J. Phys. Chem. B **111**, 9046 (2009).